Research article

Performance and usefulness evaluation of a software-based scatter correction technique for mammographic images

Kyuseok Kim [a],[1], Eun Il Cho [b],[1], Hyun-Woo Jeong [a],[*], Youngjin Lee [c],[**]

[a] *Department of Biomedical Engineering, Eulji University, Seongnam-si, Republic of Korea*
[b] *VRAD Inc., A708, Hyundai Knowledge Industry Center 2nd, Republic of Korea*
[c] *Department of Radiological Science, Gachon University, Incheon, Republic of Korea*

ARTICLE INFO

ABSTRACT

Although physical grids improve contrast in radiographic images by reducing scattered radiation, various artifacts such as grid shadow, moire, and cutoff result in increased patient doses. To overcome these problems, this study evaluates the applicability and usefulness of a material thickness-based scatter-correction technique for mammography. Specifically, this study aims to compare and evaluate the performance of mammography using the proposed software-based scatter correction framework and a physical grid. The proposed technique enables scatter correction based on pre-calculated parameters of a thickness-based scatter kernel at a water slab phantom and an empirical quantity of scatter components in a mammographic system. In the Monte Carlo simulation and experiment, the proposed framework displayed an intensity profile and full width at half maximum that closely approximated those seen in the physical grid. In addition, by applying the proposed framework to the ACR phantom, it was verified that all structures, including specks, were distinctly distinguished. The results demonstrate that the X-ray scatter-correction method with a software-based framework for mammography is applicable to the field of diagnostic imaging, as this approach yields image quality equivalent to that achieved with physical grids while also enabling a reduction in radiation doses for patients.

1. Introduction

The incidence of cancer is steadily increasing on a global scale, with breast cancer being the most prevalent malignancy and a leading cause of mortality among women [1–3]. Furthermore, Fitzmaurice et al. found that breast cancer is a leading cause of death and disability-adjusted life years (DALYs), accounting for 601,000 deaths and 17.4 million DALYs in 2017 [4]. Therefore, breast cancer screening is crucial for the early detection of masses and microcalcifications [5].

As a standard X-ray imaging technique used in clinics, digital mammography plays a key role in screening and detecting breast cancer [5]. Conventional digital mammographic systems typically comprise an X-ray tube (e.g., W/Rh and W/Ag target filter),

high-resolution detector, and compression paddle [6,7]. The recommended average glandular dose is less than 2.5 mGy per projection [8].

In mammographic examinations, contrast loss inherently occurs because of the superposition of tissue components (e.g., glandular and fatty tissue) in the projection image [9] and radiation scattering [10]. The compression paddle is used to improve image quality and reduce the absorbed dose [11]. Breast compression prevents motion blur and reduces the superimposition of lesions owing to separate tissue structures. Scatter removal is critical factor; the amount of radiation scattered decreases with thickness when the object reacts. The degradation caused by scatter is generally calculated using Eq. (1) [12]:

$$g(x,y) = I_p(x,y) + I_s(x,y), \tag{1}$$

where $g(x,y)$ is the degraded image with a primary component $I_p(x,y)$ and scatter component $I_s(x,y)$ in the Cartesian coordinate system. Here, $I_s(x,y)$ can be used for various mathematical-physical models, and a scatter point-spread function (sPSF) is most commonly used. The representative sPSF-based model is expressed by Eq. (2), as follows:

$$I_s(x,y) = I_p(x,y) \bigotimes\bigotimes sPSF(x,y), sPSF(r) = \frac{\delta(r)}{r} + \frac{SF}{(1-SF)2kr}e^{-r/k}, SF = \frac{I_s(x,y)}{I_p(x,y) + I_s(x,y)}, \tag{2}$$

where $\bigotimes\bigotimes$ is a two-dimensional (2D) convolution operator, and $I_s(x,y)$ can be simply expressed by convolving $I_p(x,y)$ and $sPSF(x,y)$ in a shift-invariant system [13]. $\delta(r)$ is the delta function of the primary transmission component at a radial distance r, and k is the mean propagation distance of scatter radiation. According to the study by Boone and Seibert, these two terms balance according to signal strength and object thickness. Detailed descriptions of the symmetric $sPSF(x,y)$ can be found in Refs. [14,15].

Mechanical breast compression techniques fail to sufficiently eliminate scattered radiation and often cause discomfort and pain during and after examination [16]. An alternative approach to eliminating scatter radiation is the hardware-based scatter-rejection method. The air-gap technique [17] is a method in which the distance between the X-ray source and detector is maximized to prevent scattered radiation from entering the detector. Although this approach does not require additional devices, its constrained geometry presents limitations. The grid technique [18] is the most widespread method owing to its outstanding performance in terms of scatter rejection. This approach is primarily designed so that 1D or 2D lead strips absorb scattered radiation while aluminum and carbon graphite fill the space between them. However, the image quality degrades because of grid shadows and moire artifacts [19]. The moving grid technique prevents artifact generation via sophisticated grid motion against X-ray exposure time [20].

The grid-based scatter-rejection method incurs an essential limitation in that additional X-ray exposure is required to maintain imaging performance by absorbing radiation in the grid. Recently, several studies have focused on restoring degraded images without a physical grid. A virtual grid software (Fujifilm, Tokyo, Japan) has been developed to suppress scatter using prior information according to exposure conditions. It is also possible to set various grid conditions according to a practical setting [21]. Diagnostic accuracy was improved by using deep-learning-based SimGrid software (Samsung, Seoul, South Korea) in low-dose pediatric radiographic images to increase the visibility of foreign materials and bones [22]. Learning-based scatter correction methods digitally restore X-ray images by removing scatter based on information of scatter radiation (e.g., scatter amplitude, distribution, etc.). Thus, no artifacts are generated and there is an advantage in reducing the radiation dose to the patient. However, these approaches have limitations in that they need large clinical datasets and require further validation to verify the reproducibility of the software in multi-modality applications.

Star-Lack et al. [23] introduced the prior-information-based scatter-correction method, which pre-calculates the scatter kernel and amplification according to the thickness of the water slab phantom using system modeling in Monte-Carlo (MC) simulation based on experimental conditions. Based on this, the sPSF presented by Ohonesorge et al.'s model [24] is fitted, and then the primary image without the scatter component is estimated. The method proved highly effective in removing scatter radiation in X-ray cone-beam computed tomography. However, the parameters of Ohonesorge et al.'s model were estimated by dividing the group into three thickness categories to satisfy the prescribed model shape, which reduces accuracy. Moreover, the high-frequency noise components in the degraded image were amplified by Fourier-transform-based direct inverse filtering using the estimated scatter kernels.

Continuing the R&D, a water-equivalent thickness kernel-based scatter-correction method incorporating total variation (TV) regularization was investigated and its viability in mammographic imaging systems was evaluated. The imaging performance between the proposed algorithm and physical grid was compared, and a systematic simulation and experiment were performed to demonstrate the feasibility of the proposed approach. In the following sections, the proposed scatter-correction software scheme is briefly described, and the experimental results are presented.

2. Materials and methods

2.1. Proposed software-based scatter-correction framework

To correct the scatter component, the proposed software requires prior sPSF information based on the thickness of the basis material. Each sPSF was measured using the MC simulation under equivalent conditions to those used in the experiment: tube voltage of 29 kV$_p$ as a pencil beam and filtration of 5.543 mm Al. Water was used as the basis material, and 10 sets of water slabs with a thickness of 30 mm were employed. In addition, 100 scatter kernels according to the i-th thickness (TK_i)—defined in Eq. (3)—were obtained at each 1-mm thickness.

$$TK_i = SF_w(i)PSF(i), \tag{3}$$

where $SF_w(i)$ and $PSF(i)$ are the empirical compensation factors for scatter kernel amplitude and point-spread function (PSF) at i-th thickness for scatter kernel distribution, respectively. The TK_i was previously measured using the MC simulation, and which is 2D low-pass filter. We redefine Eq. (2) by applying a factor for the thickness as in Ref. [23]:

$$I_s(x,y) = \sum_{i=1}^{100} \sum_{n=1}^{N} \sum_{m=1}^{M} I_p(x_m, y_n) TK_i(x - x_m, y - y_n) \tag{4}$$

where x_m, y_n denote pixel coordinates and the maximum distribution is the matrix size of input image, M and N. In order to apply the TK_i, a pixel-by-pixel thickness calculation is required for the degraded image, g. The segmentation mask according to the i-th thickness is defined as follows.

$$Mask_i(x,y) = \begin{cases} True, thickness_i \leq \tau(x,y) \leq thickness_{i+1} \\ False, otherwise \end{cases} \tag{5}$$

$$\tau(x,y) \approx \frac{1}{\mu_{water}} ln\left(\frac{I_0(x,y)}{I_p(x,y)}\right) \tag{6}$$

In Eq. (6), τ is the water-equivalent thickness when replacing the projection image with a pre-obtained projection image using a water slab, μ_{water} is the linear attenuation coefficient of water, and $I_0(x,y)$ is the measured scatter-free component without an object. The initial $I_p(x,y)$ is calculated from the degraded image $g(x,y)$, and the $\tau(x,y)$ is calculated by the updated $I_p(x,y)$ through the proposed framework. This is done equally in simulation and experiment.

From the above equations, we propose a framework to compensate for the scatter radiation, as illustrated in Fig. 1. Briefly, obtain the degradation image, g, using a mammography system without physical grid (①). Then, measure the thickness-specific scatter kernel, TK_i, through the MC simulation (②). The initial scatter component, $I_s^{(1)}(x,y)$, is then calculated using Eqs. (4)–(6) in the proposed thickness based scatter-correction framework (③). Here, the initial $I_p^{(0)}(x,y)$ used the acquired image, $g(x,y)$. And then Eq. (7) represents the process used to update the primary component $I_p(x,y)$ (④).

$$I_p^* = \underset{I_p \in Q}{\operatorname{argmin}} \varnothing(I_p), \varnothing(I_p) = \frac{1}{2}\left\|g^{(n+1)} - g\right\|_2^2 + \alpha\left\|g^{(n+1)}\right\|_{TV}, g^{(n+1)} = I_p^{(n+1)} + \lambda I_s^{(n+1)} \tag{7}$$

where Q is the set of feasible I_p, which is the $\{I_p^{(1)}, I_p^{(2)}, \ldots I_p^{(end)}\}$ updated via Eq. (7). The optimal I_p^* is considered to be the one that
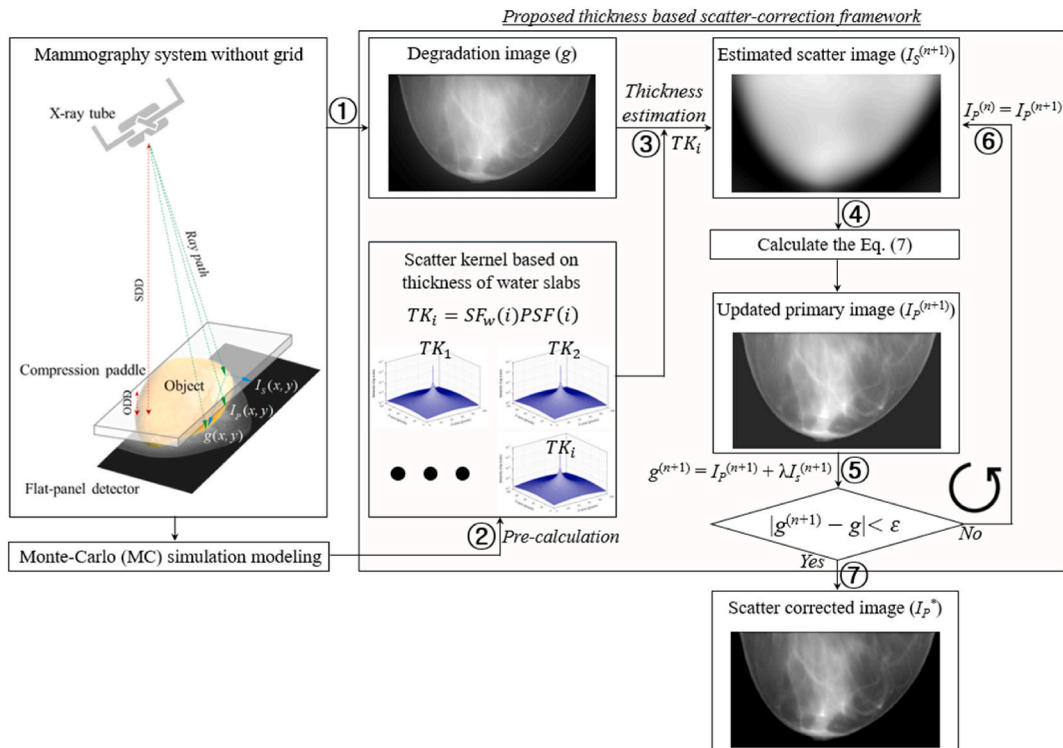

Fig. 1. Simplified schematic of the proposed framework to compensate the scatter radiation component.

minimizes the object function $\varnothing$ among the various I_p. The factor α is the balance parameter between the fidelity term and TV regularization penalty term, and λ is the balance factor to control the update step of $g^{(n+1)}$. The iteration loop is repeated until the error between $g^{(n+1)}(x,y)$ and $g(x,y)$ is below the tolerance value. Here, Eq. (7) can be solved approximately using the accelerated gradient-projection-Barzilai-Borwein (GPBB) method [25]. The proposed method minimizes the impact of noise through TV regularization and achieves accurate results through the Barzilari-Borwein (BB) step size selection in GPBB method [26]. Based on the updated primary image, $I_p^{(n+1)}$, derive the degraded image, $g^{(n+1)}(x,y)$, as in Eq. (7) (⑤). Repeat steps ④ and ⑤ after predicting the scatter image, $I_S^{(n+1)}$, using the thickness based scatter kernel and $I_p^{(n+1)}$ until the error between $g^{(n+1)}(x,y)$ and $g(x,y)$ is below the tolerance value, ε. Here, the tolerance value was used to $\varepsilon = 10^{-4}$ by trial and error (⑥). In this study, satisfactory results were empirically derived after approximately 10 iterations. Finally, the scatter corrected image, I_p^*, was derived from degraded image.

2.2. Simulation and experimental setup

Based on the aforementioned description, we implemented the proposed algorithm using the Geant4 application for tomographic emissions (GATE) software package (ver. 9.0, Geant4 10.7 patch 1, OpenGATE collaboration) and MATLAB software (ver. 8.3, MathWorks, USA), and performed a systematic simulation and experiment to evaluate the feasibility of the method. The GATE simulation was modeled to verify the usefulness of the proposed method. We modeled an X-ray imaging system with the following conditions: the X-ray tube potential was 30 kV_p at poly-energy spectrum, which was generated by the IPEM Rep78 software; the number of photons was 10^{12}; the source-to-detector distance was 65 cm; the detector pixel size was 0.1 mm and the matrix dimensions were 650 × 650 pixels; the focused grid (line density: 66 lp/mm) was positioned between the detector and object; and the examined numerical step phantom was composed of methyl methacrylate (PMMA, thicknesses: 8, 10, 12, 14, and 16 cm). The scatter kernels corresponding to 10 sets of water slabs with a thickness of 30 mm were measured in advance under the system conditions modeled in the simulation. We used an X-ray system consisting of an X-ray tube (M-113T, Varian, exposure condition: tube voltage = 29 kV_p, tube current = 45 and 60 mAs, focal spot size: 0.1 mm) and an indirect conversion-type flat-panel detector (ROSE-M Sensor, Aspenstate, pixel dimension: 3032 × 3800 pixels, pixel size: 0.076 mm). In addition, a carbon graphite-interspaced grid for mammography (JPI Healthcare, dimensions: 18 × 24 cm, line density: 103 lp/inch, ratio: 5:1, focal distance: 65 cm) was used for performance comparison purposes. Scatter correction was performed using MATLAB software based on the thickness-specific scatter kernel and the acquired degraded images through simulation and experiment. To compute the minimization problem in Eq. (7), we used the image processing toolbox and optimization toolbox of MATLAB software. We empirically applied the following parameters to solve the minimization problem in Eq. (7): balancing parameter $\alpha = 10$, balance factor $\lambda = 0.25$, and tolerance value of 10^{-4}.

Fig. 2(a) illustrates the physical phantom of an acrylic step (thickness: 8–14 cm) and Fig. 2(b) also presents the mammographic accreditation phantom (ACR phantom, serial number: AAC763, Model 015, CIRS, USA) with the inserted materials. The ACR phantom had embedded structures—including fibers, specks, and masses—in the wax insert in place of fibrous structures, microcalcifications, and tumors.

2.3. Quantitative evaluation of image performance

To evaluate the performance of the proposed method, various quantitative and qualitative analyses were performed. The full width at half maximum (FWHM) can be expressed using Eq. (8).

$$\text{FWHM} = 2\sqrt{2\ ln\ 2}\sigma, \tag{8}$$

(a)   (b)
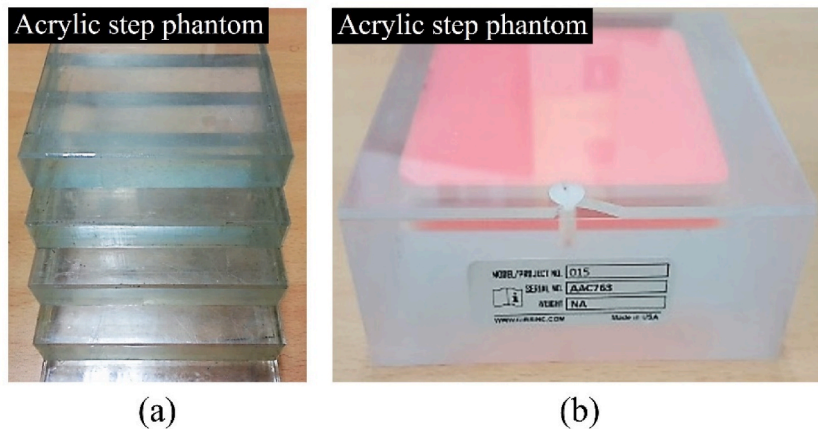
Fig. 2. Examples of (a) hand-made acrylic step phantom (thickness = 8–14 cm at five steps) and (b) mammographic accreditation phantom (ACR phantom) for experiment.

where σ is the standard deviation of the profile, which is a function of the density of the normal distribution form. Thus, we can estimate that a smaller FWHM value of the profile improves the scatter-correction effect.

The contrast-to-noise ratio (CNR) is a commonly used factor for image quality [27,28] and is defined by Eq. (9):

$$CNR = \frac{|S_{ROI_S} - S_{ROI_{BG}}|}{\sqrt{\sigma_{ROI_S}^2 + \sigma_{ROI_{BG}}^2}}$$

(9)

In Eq. (9), the parameters S_{ROI_S} and σ_{ROI_S} are the mean and standard deviation of the signal in the target region of interest (ROI), respectively, and $S_{ROI_{BG}}$ and $\sigma_{ROI_{BG}}$ are the average and standard deviation of the background signal, respectively. The objective was to investigate similarities in CNR values between a scatter-rejection image with a physical grid and one using the proposed algorithm. Larger CNR values are generally associated with higher image quality.

3. Results and discussion

Fig. 3 (a) presents a complete set using the MC simulation with a numerical PMMA step phantom of the reference image generated solely by the primary component, a scatter-rejected image with the physical grid, and a scatter-corrected image using the proposed approach. To evaluate the performance of the algorithm, Fig. 3 (b) depicts the measured intensity profiles, with line *AB* shown in Fig. 3 (a). These results indicate that the profile tendency of the proposed thickness-based scatter-correction method is more similar to that of the physical grid than that of the degraded image without a physical grid. Compared to the profile of the scatter-rejection image obtained using the physical grid, the profile of the degraded image without the physical grid shows increased intensity in the staircase
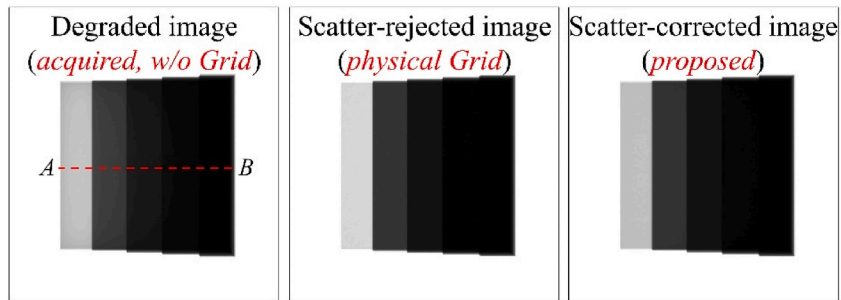
(a)
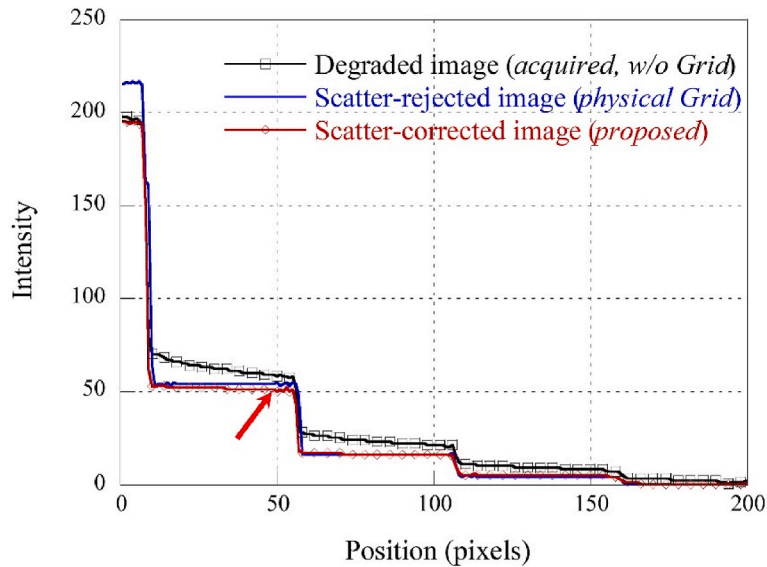
(b)

Fig. 3. Sample images of numerical PMMA step phantom using the Monte-Carlo simulation: (a) degraded image without the physical grid, scatter-rejected image with physical grid, and scatter-corrected image using the proposed method; and (b) the profiles of three images at line *AB*.

edge region, primarily due to the scatter radiation. This phenomenon is responsible for reducing the contrast of the region with respect to the height of the stair phantom. In clinical mammography, scatter radiation causes a decrease in contrast, making it difficult to distinguish tumors or small calcifications. The proposed method corrects the degraded image based on the thickness of scatter kernels. In the case of a single material object, we demonstrated that the effect on the scatter radiation was corrected based on the accurate separation of thickness and its scatter kernels, which proves that the proposed algorithm is effective in scatter radiation correction. During scatter correction, we found that some areas dropped owing to excessive compensation of thickness, as denoted by the arrows in Fig. 3 (b). However, the proposed scatter-correction algorithm was overall effective in terms of accurately estimating the scattering image from a single projection.

To verify the practical viability of the simulation results, we performed experiments using an acrylic step phantom shown in Fig. 2 (a). Fig. 4 (a) presents the imaging results of the experiment with the acrylic step phantom using the three approaches. Here, the tube current of the acquired image without a physical grid (left) was 45 mAs, whereas that of the acquired image with a physical grid (right) was 60 mAs. Fig. 4 (b) shows the intensity profiles measured along the line *CD* of the images. The intensity profile of the scatter-corrected image was closer to that of the image acquired with a physical grid than that of the scatter-rejected image without a physical grid. Consistent with the trend of the simulation results, the profile of the image acquired without a physical grid increased towards the step edge region owing to scatter radiation, which reduces the contrast of the image. The proposed scatter-correction algorithm proves viable in the experiment, obtaining a corrected image with a profile similar to that of the image using the physical grid. This result shows that it is possible to acquire high-contrast images without exposing the patient to radiation overexposure associated with the use of traditional physical grid technique. Moreover, the profile using the proposed method is less noisy compared to the profile using the physical grid. When using the physical grid, it is more irradiated than without the physical grid to compensate for the photons loss. This method increases the patient dose. The proposed method has the advantage of obtaining a contrast ratio similar to a physical grid with less radiation exposure, thus increasing CNR, an important factor in determining image quality.

To confirm the results of the quantitative evaluation, Fig. 5 shows the differential profiles from 380 to 420-pixel positions in Fig. 4 (b). Note that the FWHM of the differential profile in the scatter-corrected image was approximately three pixels, representing an approximately 1.5-times decrease from that of the scatter-rejected image with the physical grid. Furthermore, the FWHM value of the degraded image was approximately five pixels. Notably, these results demonstrate that the proposed method achieves a scatter compensation performance comparable to that of the physical grid. However, the proposed algorithm incurs an overshoot, as indicated by the red arrows in Fig. 4 (a), when the scatter kernel prediction according to object thickness is set too high compared to that of the
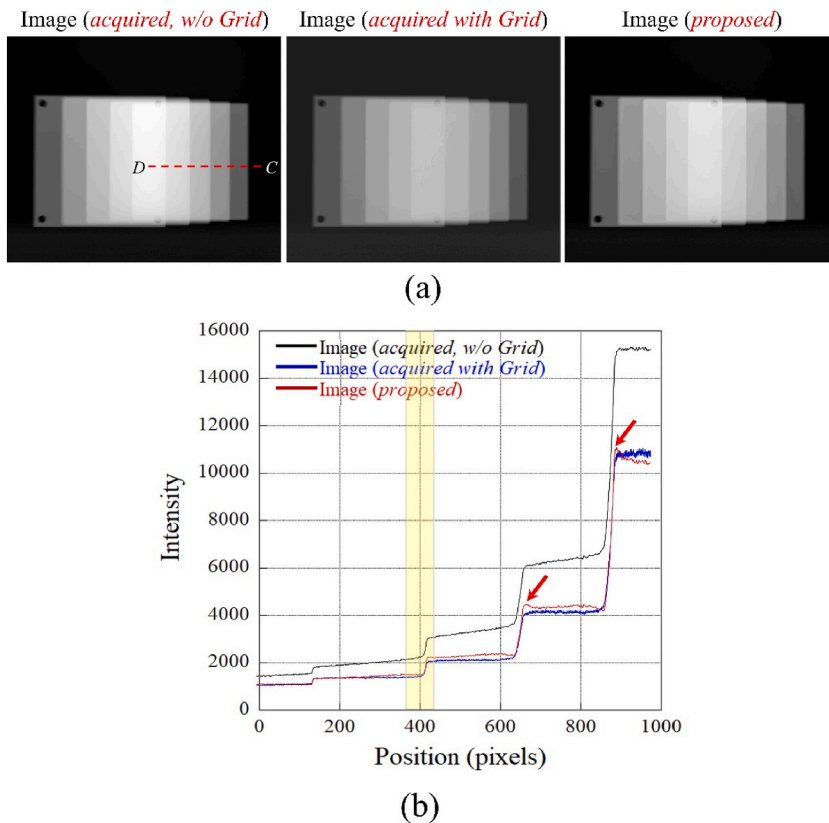

Fig. 4. (a) Experimental results of an acquired image without a grid, a scatter-rejected image with a physical grid, and an image using the proposed method; (b) intensity profiles as measured along the line *CD*.
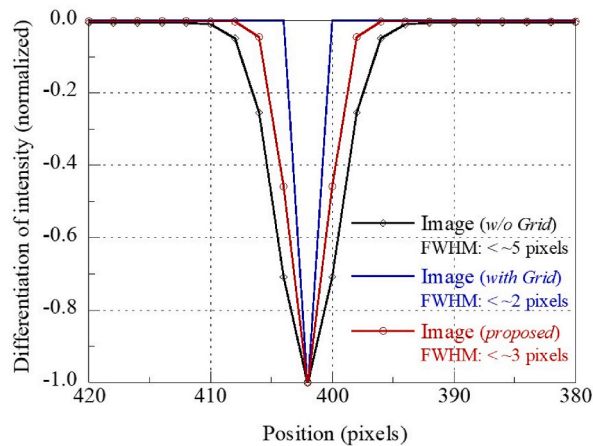
Fig. 5. Differential profiles and FWHM values from 380 to 420 position (pixels) in Fig. 4 (b).

real object.

Fig. 6 (a) presents experimental imaging results of the acquired image without the physical grid, acquired image with the grid, and restored image using the proposed method. Fig. 6 (b) shows the enlarged images indicated by the box ROI_A in Fig. 6(a). The enlarged images can be examined to qualitatively investigate the improvement in sharpness and contrast of the speckle region by using the proposed method. Furthermore, most of the embedded structures (fibers, specks, and masses) in the ACR projection image are much more clearly visible in the proposed image, similar to the acquired physical-grid-based image. The qualitative results demonstrate that the proposed algorithm provides a significant improvement in scatter radiation, even for objects made of various materials and thicknesses. Notably, the contrast in the ROI_A increased, improving the ability to distinguish speckles, even though the proposed ACR image was acquired with a 0.75-time dose reduction compared with the image without the physical grid. This shows the ability of the proposed method to favor the identification of cancers or microcalcifications on mammograms, which is expected to improve diagnostic accuracy. We visually evaluated non-uniformity due to scatter radiation; Fig. 7 shows the profile results along the line EF in Fig. 6 (a). In terms of uniformity, the profile of the scatter-corrected image obtained using the proposed method was similar to that of
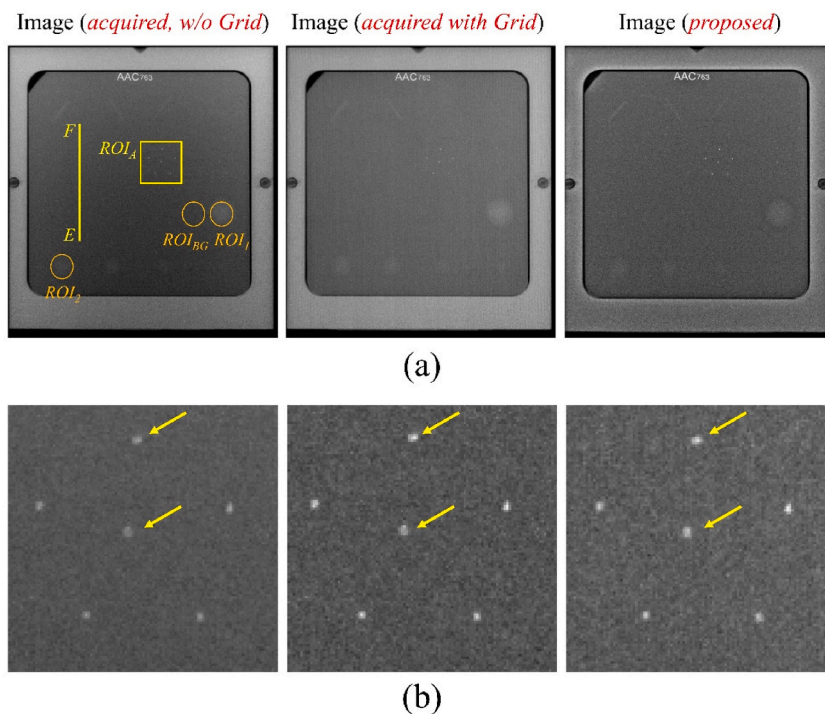

Fig. 6. Results with ACR phantom; (a) the acquired image without a grid, physical grid image, and restored image with proposed method; (b) enlarged images indicated by box ROI_A in Fig. 6 (a).

the scatter-rejection image. Despite the regions of equivalent compressed average breast having the same thickness, the uniformity of the image without the physical grid was inconsistent owing to scatter radiation. Correcting uniformity using the proposed method is critical to improving the diagnostic accuracy of mammographic images for qualitative microstructures and small lesions.

The proposed algorithm improved contrast, uniformity, and sharpness by compensating for scattered radiation. However, the problem of amplified noise following the proposed scatter correction is a limitation to image-quality improvement. Although the level of noise amplification is quite low compared to that of the direct inverse filtering method by Star-Lack et al. [23], it is essentially high-pass filtering, and this issue must be addressed. Table 1 lists the CNR values presented in Fig. 6 (a). We observe that the CNR values of the scatter-corrected image obtained using the proposed method were increased by approximately 1.2 times compared to those of the degraded image without the grid. However, compared to the CNR values of the physical grid, they were approximately 1.4 times lower. As shown in Fig. 7, noise amplification occurs when scattered radiation is removed. When the low-frequency scatter component is corrected, the variability among image values increases, which improves sharpness but amplifies noise [29]. Amplified noise is difficult to identify when the anatomical structures and noise components are indistinguishable. Recently, techniques have been proposed to reduce noise while preserving the edge structure, and we plan to apply these methods to improve the performance of the proposed method in continuous R&D [30,31].

Another limitation is the blurring artifact, which occurs owing to finite characteristics of the imaging system (such as focal spot size and detector pixel size) [32] and patient movement during mammogram exposure [33]. The blurring component can be categorized as low-frequency information, such as scatter radiation, and when the proposed method attempts to apply a thickness-specific scatter kernel to an object, inaccurate thickness measurements can prevent accurate scatter correction. Various methods have been proposed to correct blur artifacts in mammography and digital breast tomosynthesis [34,35]. We plan to apply the proposed method to further experimental and clinical validation in the future.

Finally, the error propagation probability of the algorithm for grid-line artifact removal is used as the reference image. Kykanen et al. mentioned that scattered radiation is one of the primary causes of quality degradation in mammography images [36]. A physical grid is a representative method for removing the scattered radiation that may be generated in X-ray-based images. However, the use of a grid presents the disadvantage that the exposure dose received by the patient inevitably increases owing to an increase in exposure conditions from the partial absorption of primary X-rays. Veldkamp et al. demonstrated that although the quality of mammographic images can be significantly improved using a physical grid, the exposure dose may reach a three-fold increase [37]. When the proposed scatter-corrected method is used instead, we expect that it will be possible to simultaneously improve imaging quality and decrease the exposure dose for the patients. Therefore, we chose the reference image using the physical grid. However, the grid-line artifacts in Fig. 6 (a) can be observed in the image acquired with a physical grid. These artifacts, which are caused by the grid shadow, reduce the accuracy of lesion detection in mammographic images. Because grid-line artifacts are a critical part of quality control, periodic testing is specified by the Mammography Quality Standards Act (MOSA) [38]. These artifacts were not prominent in the physical grid-based X-ray images examined in this study owing to the removed components of grid-line artifacts in the Fourier domain. The existing grid-line removal filtering methods, including the windowed adaptive switching minimum filters, adaptive optimum notch filters, and adaptive Gaussian notch filters, were applied to the image with the physical grid [39–41]. Based on these algorithms, effective grid-line removal was performed; however, a high-frequency blurring artifact occurred due to the resolution loss during the grid-line artifact removal. This may affect the results obtained and have a negative impact on the accuracy of deep-learning training for scatter correction. In the future, we plan to perform a comparative evaluation between scatter-corrected technology and various existing software technologies, including the automated grid-artifact-detection algorithm proposed by MacLellan et al. [38]. Extended clinical studies using multi-modality imaging systems will examine the clinical applicability of the proposed algorithm. It is expected that efficient mammography examinations can be performed in clinical practice.

Image-guided biopsy is widely employed in diagnostic medicine when breast imaging findings include mammography [42]. Among breast tissue biopsy techniques, the stereotactic-based method is known to be well-validated, and radiologists often use grids to identify target areas. Mango et al. studied the effect of grid-based breast X-ray images on the efficiency of stereotactic biopsy [43]. As a result, an increase in the stereotactic biopsy efficiency was confirmed with an increase in total procedure time and the exposure dose, when the grid was used. We therefore expect that the physical grid time and table time can be reduced by applying the software-based grid, as proposed in this study, to stereotactic biopsy. Consequently, we expect the accuracy of biopsy to improve without increasing exposure.

4. Conclusion

The objective of this study was to achieve effective scatter correction based on software used in conventional mammography without a physical grid. The software predicts and eliminates scatter components from acquired images; the prior scatter kernel is repeatedly calculated until the difference between the preceding and current restored images is below a threshold value. Here, the scatter kernels were calculated using a water phantom according to thickness. We investigated the proposed software and performed a systematic simulation and experiment to demonstrate its viability. The uniformity of a scatter-corrected image was closer to that of a scatter-rejected image with a physical grid than that of a degraded image without a grid. In particular, the FWHM value of a scatter-corrected image was approximately 1.5 times smaller than that of the corresponding scatter-rejected image. Furthermore, the CNR factor of the proposed image was approximately 1.2 times higher than that of the degraded image. These results demonstrate the efficiency of the proposed framework in compensating for the scatter components in mammography. Furthermore, the proposed method is expected to produce satisfactory results for scatter correction using various radiographic imaging modalities.
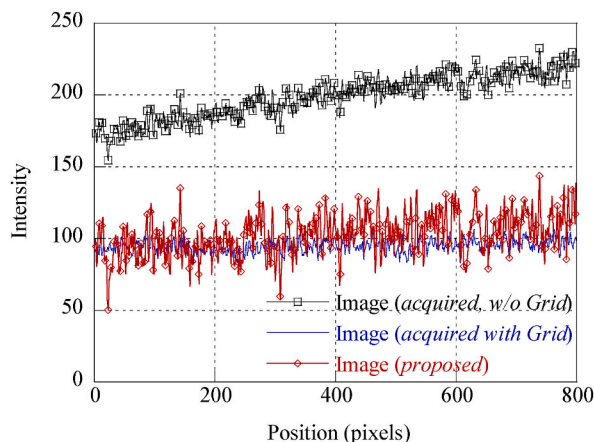
Fig. 7. Measured profiles of acquired images without a grid, with a grid, and scatter correction using the proposed method, indicated by line *EF* in Fig. 6 (a).

Table 1
CNR results using the ACR phantom in Fig. 6 (a).

Region	Degraded (without grid)	Scatter-rejected (physical grid)	Scatter-corrected (proposed)
ROI$_1$	7.15 ± 0.41	13.93 ± 0.11	8.36 ± 0.83
ROI$_2$	3.24 ± 0.62	5.12 ± 0.10	3.95 ± 0.21

CRediT authorship contribution statement

Kyuseok Kim: Writing – original draft, Software, Methodology, Formal analysis, Conceptualization. **Eun Il Cho:** Writing – original draft, Investigation. **Hyun-Woo Jeong:** Writing – review & editing, Formal analysis. **Youngjin Lee:** Writing – review & editing, Software, Formal analysis, Conceptualization.

Declaration of competing interest

The authors declare that they have no known competing financial interests or personal relationships that could have appeared to influence the work reported in this paper.

References

[1] B.O. Anderson, A.M. Ilbawi, E. Fidarova, E. Weiderpass, L. Stevens, M. Abdel-Wahab, B. Mikkelsen, Lancet Oncol. 22 (2021) 578, https://doi.org/10.1016/S1470-2045(21)00071-1.
[2] Global burden of disease cancer collaboration, JAMA Oncol. 5 (2019) 1749, https://doi.org/10.1001/jamaoncol.2019.2996.
[3] M. Kang, Y.S. Chun, H.K. Park, E.K. Cho, J. Jung, Y. Kim, Annals of Surgical Treatment and Research 102 (2022) 73, https://doi.org/10.4174/astr.2022.102.2.73.
[4] D.M. Vo, N.Q. Nguyen, S.W. Lee, Inf. Sci. 482 (2019) 123, https://doi.org/10.1016/j.ins.2018.12.089.
[5] S.M. Friedewald, E.A. Rafferty, S.L. Rose, M.A. Durand, D.M. Plecha, J.S. Greenberg, M.K. Hayes, D.S. Copi, K.L. Carlson, T.M. Cink, L.D. Barke, L.N. Greer, D.P. Miller, E.F. Conant, JAMA 311 (2014) 2499, https://doi.org/10.1001/jama.2014.6095.
[6] L.B. Nogueira, T.P.R. Campos, D.P.M. dos Santos, P.M.C. de Oliveira, C.C.P. Fontainha, Radiat. Phys. Chem. 193 (1999) 109971, https://doi.org/10.1016/j.radphyschem.2022.109971.
[7] N. Moshina, S. Sebuødegård, K.T. Evensen, C. Hantho, K.A. Iden, S. Hofvind, Eur. J. Radiol. 115 (2019) 59, https://doi.org/10.1016/j.ejrad.2019.04.006.
[8] K.C. Teoh, H.A. Manan, N.M. Norsuddin, I.H. Rizuana, Healthcare 9 (2021) 1758, https://doi.org/10.3390/healthcare9121758.
[9] M. Dustler, I. Andersson, D. Förnvik, A. Tingberg, Proc. SPIE 8313, Physics of Medical Imaging 8313 (2012) 83134M, https://doi.org/10.1117/12.905746. *Medical Imaging 2012*.
[10] S.M. Leon, L.F. Brateman, L.K. Wagner, Med. Phys. 41 (2014) 061901, https://doi.org/10.1118/1.4873321.
[11] R.S. Saunders Jr., E. Samei, Med. Phys. 35 (2008) 4464, https://doi.org/10.1118/1.2977600.
[12] J.L. Ducote, S. Molloi, Phys. Med. Biol. 55 (2010) 1295, https://doi.org/10.1088/0031-9155/55/5/003.
[13] P. Monin, F.R. Verdun, H. Bosmans, S.R. Pérez, N.W. Marshall, Phys. Med. Biol. 62 (2017) 5691, https://doi.org/10.1088/1361-6560/aa75bc.
[14] J.M. Boone, J.A. Seibert, Med. Phys. 15 (1988) 721, https://doi.org/10.1118/1.596186.
[15] J.M. Boone, K.K. Lindfors, V.N. Cooper 3rd, J.A. Seibert, Med. Phys. 27 (2000) 2408, https://doi.org/10.1118/1.1312812.
[16] G.A. Agasthya, E. D'Orsi, Y.J. Kim, P. Handa, C.P. Ho, C.J. D'Orsi, Am. J. Roentgenol. 209 (2017) W322, https://doi.org/10.2214/AJR.16.17615.
[17] U. Neitzel, Med. Phys. 19 (1992) 475, https://doi.org/10.1118/1.596836.
[18] H.P. Chan, K. Doi, Phys. Med. Biol. 27 (1982) 785, https://doi.org/10.1088/0031-9155/27/6/002.
[19] D.M. Gauntt, G.T. Barnes, Med. Phys. 33 (2006) 1668, https://doi.org/10.1118/1.2184444.
[20] D.S. Kim, S. Lee, Med. Phys. 40 (2013) 061905, https://doi.org/10.1118/1.4807085.
[21] T.M. Gossye, P.V. Smeets, E. Achten, K. Bacher, Invest. Radiol. 55 (2020) 374, https://doi.org/10.1097/RLI.0000000000000646.

[22] P.C. Krueger, K. Ebeling, M. Waginger, K. Gluting, M. Scheithauer, P. Schlattmann, H. Proquitté, H.J. Mentzel, Pediatr. Radiol. 52 (2022) 1029, https://doi.org/10.1007/s00247-021-05279-2.

[23] J. Star-Lack, M. Sun, A. Kaestner, R. Hassanein, G. Virshup, T. Berkus, M. Oelhafen, Proc. SPIE 7258, medical imaging 2009, Physics of Medical Imaging 72581Z (2009), https://doi.org/10.1117/12.811578, 12 March 2009.

[24] B. Ohnesorge, T. Flohr, K. Klingenbeck-Regn, Eur. Radiol. 9 (1999) 563, https://doi.org/10.1007/s003300050710.

[25] J. Barzilai, J.M. Borwein, IMA J. Numer. Anal. 8 (1988) 141, https://doi.org/10.1093/imanum/8.1.141.

[26] J.C. Park, B. Song, J.S. Kim, S.H. Park, H.K. Kim, Z. Liu, T.S. Suh, W.Y. Song, Med. Phys. 39 (2012) 1207, https://doi.org/10.1118/1.3679865.

[27] M.J. Tapiovaara, R.F. Wagner, Phys. Med. Biol. 38 (1993) 71, https://doi.org/10.1088/0031-9155/38/1/006.

[28] M. Koutalonis, H. Delis, G. Spyrou, L. Costaridou, G. Tzanakos, G. Panayiotakis, Phys. Med. Biol. 52 (2007) 3185, https://doi.org/10.1088/0031-9155/52/11/017.

[29] L. Zhu, J. Wang, L. Xing, Med. Phys. 36 (2009) 741, https://doi.org/10.1118/1.3063001.

[30] C. Park, Y. Lee, Nucl. Instrum. Methods Phys. Res. Sect. A Accel. Spectrom. Detect. Assoc. Equip. 1031 (2022) 166570, https://doi.org/10.1016/j.nima.2022.166570.

[31] S.W. Cheng, Y.T. Lin, Y.T. Peng, Sensors 22 (2022) 926, https://doi.org/10.3390/s22030926.

[32] S. Tilley, J.H. Siewerdsen, J.W. Stayman, Phys. Med. Biol. 61 (2016) 296, https://doi.org/10.1088/0031-9155/61/1/296.

[33] W.R. Geiser, T.M. Haygood, L. Santiago, T. Stephens, D. Thames, G.J. Whitman, Am. J. Roentgenol. 197 (2011) W1023, https://doi.org/10.2214/AJR.10.7246.

[34] N.V. Slavine, S. Seiler, T.J. Blackburn, R.E. Lenkinski, Proc. SPIE 10574, Medical Imaging 2018: Image Process. 105740G (2018), https://doi.org/10.1117/12.2293604, 2 March 2018.

[35] A.M. Mota, M.J. Clarkson, P. Almeida, N. Matela, IEEE Trans. Med. Imag. 39 (2020) 4094, https://doi.org/10.1109/TMI.2020.3013107.

[36] K. Nykänen, S. Siltanen, Med. Phys. 30 (2003) 1864, https://doi.org/10.1118/1.1584160.

[37] W.J.H. Veldkamp, M.A.O. Thijssen, N. Karssemeijer, Med. Phys. 30 (2003) 1712, https://doi.org/10.1118/1.1584044.

[38] C.J. MacLellan, R.R. Layman, W. Geiser, D.A. Gress, A.K. Jones, Med. Phys. 46 (2019) 3442, https://doi.org/10.1002/mp.13621.

[39] P. Moallem, M. Masoumzadeh, M. Habibi, Signal, Image and Video Processing 9 (2015) 1179, https://doi.org/10.1007/s11760-013-0560-0.

[40] J. Varghese, S. Subash, N. Tairan, IET Image Process. 10 (2016) 646, https://doi.org/10.1049/iet-ipr.2015.0750.

[41] J. Varghese, S. Subhash, K. Subramaniam, K.P. Sridhar, IET Image Process. 14 (2020) 1529, https://doi.org/10.1049/iet-ipr.2018.5707.

[42] M.J. Vandromme, H. Umphrey, H. Krontiras, J. Surg. Oncol. 103 (2011) 299, https://doi.org/10.1002/jso.21795.

[43] V.L. Mango, D. D'Alessio, E.A. Morris, R. Ha, B. Bernard-Davila, M.S. Jochelson, Clin. Imag. 53 (2019) 108, https://doi.org/10.1016/j.clinimag.2018.10.007.